

Flow over 50° Delta Wings with Different Leading-Edge Radii

N.G. Verhaagen¹

Delft University of Technology, Delft, 2600 GB, The Netherlands

The experimental study focuses on the effects of the leading-edge radius on the flow over 50° swept delta wing models. Three models were tested, one model has a sharp leading edge and two other have a semi-circular leading edge of different radius. The vortical flow on and off the surface of the models was investigated using an oil-flow visualization and a Stereo Particle Image Velocimetry (SPIV) technique. The leading-edge radius is shown to affect the location, size and strength of the vortices and also the vortex core breakdown location over the models. As a result of this, the forces and moment acting on a 50° delta wing are also affected. The study further shows that the structure of the flow over such a wing is weakly dependent on Reynolds number.

Nomenclature

C_D	=	drag coefficient
C_L	=	lift coefficient
C_m	=	pitching-moment coefficient
C_T	=	tangential-force coefficient
c	=	root chord length
r_{le}	=	leading-edge radius
Re	=	Reynolds number, based on chord length
s	=	local semispan
t	=	wing thickness
V_{axial}	=	axial-velocity component
V_{axis}	=	velocity component along vortex axis
V_{swirl}	=	swirl-velocity component
V_{∞}, V_{inf}	=	free stream velocity
x	=	chordwise distance
x_m	=	measurement plane coordinate
y	=	spanwise distance
y_m	=	measurement plane lateral coordinate
z	=	vertical distance from wing surface
α	=	angle of attack
Λ	=	leading-edge sweep angle

I. Introduction

In recent years much attention is given to designs of unmanned combat aircraft vehicles (UCAV). These are required to have a low structural-weight-to-take-off-weight-ratio, a large surface area to include internal flight systems and be capable of operating at high angles of attack. Concepts of this type of aircraft incorporate a so-called non-slender delta wing, or a delta wing with a leading-edge sweep angle $\Lambda < 60^\circ$.

The past 50 years, most research on delta wings was performed using so-called slender delta wings with a $\Lambda \geq 60^\circ$. Over the past years, a reasonably well understanding of the flow phenomena over this type of wing has been obtained. The structure of the flow over a non-slender delta wing differs substantially from that over a slender delta wing.¹ A

¹ Senior Research Scientist, Senior Member AIAA, Faculty of Aerospace Engineering, Kluyverweg 1, P.O. Box 5058.

reduction of Λ from, e.g., 65° to 50° results in the formation of the primary vortex much closer to the wing surface and consequently a stronger interaction between this vortex and the wing boundary layer. Gordnier and Visbal², and Chen and Wang³ predict that as a result of this interaction, at small α the primary vortex splits up into two separate regions of vorticity. This so-called dual primary-vortex core structure is confirmed in experiments performed by Taylor et al.⁴ As a result of the strong interaction, the vortex crossflow structure is sensitive to the Reynolds number, which is not the case for the vortex flow over slender delta wings. Wang and Zhang⁵ observed that dual-vortical structures can not be formed at Re below 10^4 because of high viscosity. At larger Re , they observed a dual-vortical structure to exist at α up to 10° . At higher α , the distance between the primary vortices and the boundary layer on a non-slender delta wing has increased such that only a single primary vortex develops and the cross flow structure then becomes similar to that over a slender delta wing.

Another difference is in the development of the breakdown of the vortex core. On a slender delta wing, this flow phenomenon is caused by the mutual interaction between the primary vortices over the port- and starboard wing halves. In most experiments,⁶ a sudden deceleration and even reversal of the axial velocity is observed in the core downstream of the breakdown point. This is accompanied with a spiral movement of the core which after a certain chord lengths degenerates into a turbulent wake flow. Compared to a slender delta wing, the primary vortices over a $\Lambda = 50^\circ$ delta wing are further apart from each other, hence there is less interaction between the vortices on both wing halves. Instead, the vortices are smaller and located closer to the wing. Due to the latter, a stronger interaction exists with the upper-surface boundary layer.

For the flow over the wing used in the experiments conducted by Taylor et al⁴, a couple of numerical solutions are available. It should be noted that the leading edges of their wing have a rather large bottom-edge bevel angle of 45° .

Chen and Wang³ compute the development of the core flow at $\alpha = 8^\circ$ and at $Re = 2.74 \times 10^5$. The flow is modeled using unsteady compressible Navier-Stokes equations and assuming laminar flow conditions. From the apex, the value of the velocity component along the vortex axis V_{axis} is predicted to rapidly increase to a value of about $1.6 V_\infty$ at $x/c = 0.02$. More downstream, the jet-like axial velocity reduces gradually to a value of $1.0 V_\infty$ at $x/c = 0.7$, while more downstream a wake-like axial flow profile is evident with an axial velocity rapidly decreasing to zero at the trailing edge. The computations suggest three stages of axial-velocity development, i.e., a rapid increase to a peak value, a decrease and a rapid reduction. These stages are associated with initially a strong jet-like flow, followed by a decay in core velocity and eventually a wake-like flow (breakdown). The peak value of the axial velocity is predicted to increase with α . As far as Re is concerned, $V_{axis} > V_\infty$ when $Re > 10^5$, giving evidence of a jet-like flow. However, at lower Re a wake-like flow is predicted to exist.

Gordnier et al⁷ give a numerical solution for the development of the core flow over the same delta wing at $\alpha = 15^\circ$ and at Re ranging from 2.0×10^5 to 2.0×10^6 . Solutions of the time-dependent compressible Navier-Stokes equations are obtained using a higher-order method. At the lower Re , at $x/c = 0.14$ a mean peak axial velocity of $2.91 V_\infty$ is predicted in the core. With increasing Re , this velocity decreases to a value of $2.21 V_\infty$. The onset of breakdown is identified by a switch in the core from jet-like to wake-like flow. No flow reversal is predicted as observed on slender delta wings

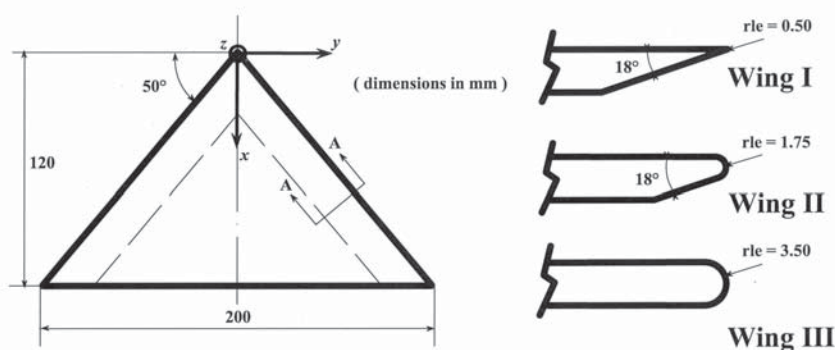


Figure 1. Planform and leading-edge shapes of small-scale models

downstream of the breakdown point. The Reynolds number is predicted to also have an effect on the breakdown location, but interestingly not always in the same sense. Associated with this is an effect on the transition of the flow in the breakdown region.

dual primary vortex structure the outboard vortex was observed to breakdown upstream of the primary vortex. The flow over a 50° delta wing was further found to be less steady than that over a slender wing; at low α fluctuations of the order of 50 % root chord were observed.

Taylor et al⁴ investigated the variation of the breakdown point with the angle of attack in a water tunnel at $Re = 13,000$. Breakdown was observed to occur already at $\alpha = 2.5^\circ$. The breakdown point moves upstream with increasing angle of attack. In the case of a

In the present research project special attention is paid to the effects of the leading-edge radius on the aerodynamic characteristics of the vortex flow. In the majority of wind tunnel experiments, delta wing models are tested that have sharp edges. These are applied to fix the boundary-layer separation at these edges and to reduce Reynolds number sensitivity effects. Realistic applications, however, often have blunt edges.⁸

For the case of a slender delta wing ($\Lambda \geq 60^\circ$), a number of experimental and numerical studies⁹⁻¹⁶ are available that discuss the effects of the leading-edge shape on the aerodynamic characteristics. These studies show that the edge shape affects the origin and location of the primary-separation line, the size and position of the primary vortex and through mutual interaction with the wing boundary layer the generation of a secondary vortex and possibly a tertiary vortex. The size and strength of the primary vortex tends to reduce with increasing leading-edge radius r_{le} . Balance measurements show that an increase in r_{le} decreases the lift only slightly, but reduces the drag significantly. The latter is due to an increase in the suction at the edges. This results into a higher lift-to-drag ratio, hence a better performance of the delta wing at subsonic speeds. Contrary to a sharp leading edge, however, on a rounded edge the location of the primary-separation line and separated flow structure are sensitive to the Reynolds number. The edge curvature also affects the location of the bursting point over the wing; an increase in r_{le} is found to move the bursting point in a downstream direction.

As far as the effects of the leading-edge radius on the characteristics of a non-slender delta wing are concerned, balance data¹⁷ suggest that the shape of the leading edge has a substantial effect on the measured lift and on the stall behavior, in other words, on the location and strength of the vortices and their breakdown location. Only little data is available on the effects on the flow itself over such wings. To be able to study these effects, at the Faculty of Aerospace

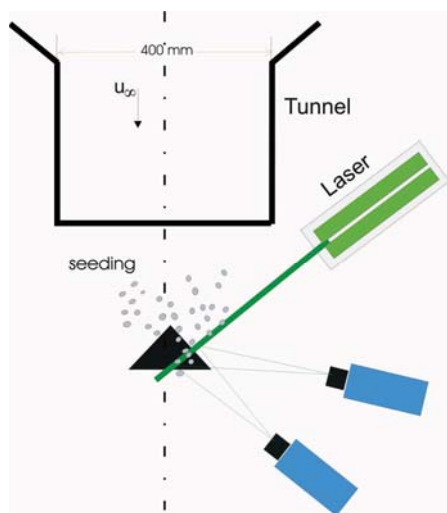


Figure 2. SPIV setup for cross flow surveys

Engineering of the Delft University of Technology (TUD) in the Netherlands, a series of three small-scale $\Lambda = 50^\circ$ delta wing models was constructed. One model has a “sharp” leading edge, while the other two models have a semi-circular edge of increasing radius. As a start, the flow on the model surface was studied using an oil-flow visualization technique, and surveys of the flow in two crossflow planes were performed using a PIV technique. These preliminary tests were performed in a small open wind tunnel and the results have been reported in a previous paper.¹⁸ The oil-flow visualization study showed a clear effect of r_{le} on the location of the secondary-separation line; a larger radius delays the outward bending of the secondary-separation line, which is indicative for a delay in the occurrence of vortex bursting over the models. The PIV data showed that a larger r_{le} reduces the size and strength of the primary vortex and moves this vortex outboard and closer to the wing surface. In addition, a slight increase in the level of the axial vorticity in the free shear layer is noted at a short distance from the leading edge. This suggests that the leading edge shape affects the direction of the local vorticity vector.

In the present paper, the abovementioned experimental data are summarized and new recently obtained data are added. These data comprise flowfield surveys obtained in a larger number of crossflow planes and flow data generated in a plane through the vortex axis. The data were obtained using a SPIV setup. In addition, balance data are presented that were obtained on a series of larger models.

II. Experimental Setup

The tests with the small-scale models were conducted in an open-jet wind tunnel with the advantage to have an easy access to the models and SPIV (Stereo Particle Image Velocimetry) equipment. Recently, a series of three times larger models have been constructed that are tested in a larger closed-circuit low-turbulence tunnel. The first tests performed with these models are the balance measurements described below.

A. Models and Flow Facility used for SPIV and Surface-Flow Visualization Tests

Three models of a $\Lambda = 50^\circ$ delta wing were manufactured of 7-mm thick anodized Aluminum. Chord length amounts .120 m and the span equals .200 m. Figure 1 shows the wing planform and the different leading-edge shapes that were selected. It should be remarked here that in principle various edge-shape combinations are conceivable, such as

symmetrical edges, edges beveled on the upper surface, etc. For the present research project, edges with a bottom-surface bevel were chosen in order to keep the upper surface of the models as flat as possible (similar edge geometries are used in other studies¹⁻⁴). Wing I has a “sharp” leading edge of 0.50 mm radius, yielding an r_{le}/c ratio of 0.0042. For practical reasons, a smaller edge radius was not applied. The edge is beveled on the bottom side at 18° . Wing II has a semi-circular leading edge of 1.75 mm radius ($r_{le}/c = 0.0149$) and wing III a semi-circular edge of 3.50 mm radius ($r_{le}/c = 0.0298$), being half the model thickness. The radius of the rounding at the model nose equals that of the leading edge. The models have a square trailing edge and a thickness-to-chord ratio $t/c = 0.06$.

The models were tested in an open-jet tunnel with a nozzle cross section of $40 \times 40 \text{ cm}^2$. The maximum airspeed in this tunnel amounts 30 m/s. The models were positioned at about a two chord lengths distance from the tunnel nozzle.

The models were screw mounted to a sting that was connected to a (α, β) traversing system.

The flow on and off the models has been investigated at a constant $V_\infty = 20 \text{ m/s}$, yielding an $Re = 2.0 \times 10^5$, based on chord length. An oil-film technique was used to visualize the boundary-layer flow on the leeward surface at $\alpha = 5^\circ, 7.5^\circ, 10^\circ, 12.5^\circ, 15^\circ$ and 22.5° . An SPIV technique was used to survey the flow over the models at the same free stream velocity, but due to the limited time available for the measurements, data were acquired only at $\alpha = 15^\circ$. The flow data were obtained in two test campaigns with each a different SPIV setup.

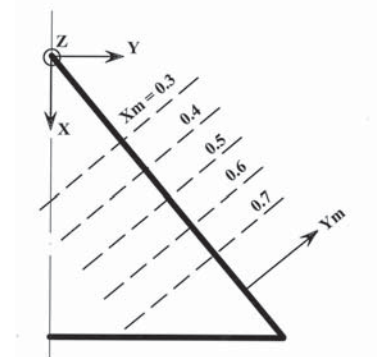


Figure 3. Schematic of SPIV measurements planes on the starboard wing half

As shown in Figure 3, the measurements were performed in five planes. The planes cross the leading edge at stations corresponding to 30 % to 70 % root chord and are denoted $x_m = 0.3$ to 0.7, respectively, where x_m is the measurement plane coordinate. A lateral coordinate y_m is defined normal to the leading-edge. The SPIV technique requires a calibration procedure to obtain the mapping function between the image coordinates and the physical space. This was obtained by using a two-level calibration pattern plate and the evaluation of the mapping function was made by LaVision DAVIS 7.1 software.

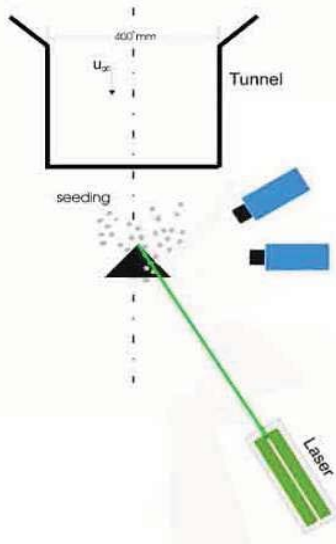


Figure 4. SPIV setup for surveys in planes through vortex axis.

B. Setups used for Flow Surveys.

Figure 2 shows the schematics of the SPIV setup used for the first test campaign. The objective of this setup was to generate crossflow data at $\alpha = 15^\circ$. Surface-flow visualization tests (to be discussed in Section III) show that the primary-attachment lines on all three wings are located well outboard of the wing centerline at this α . This suggests that there is no strong interaction between the vortices on the starboard and port half of the wings. Since the flow over the wings can therefore be assumed to be symmetric with respect to the centerline, the flow on only one wing half, the starboard wing half, was surveyed. The laser sheet illuminated the flow in planes normal to the starboard leading edge. One CCD camera was positioned normal to this sheet, while the second camera was at an angle of about 56° with the sheet. As shown in Figure 3, the measurements were performed in five planes. The planes cross the leading edge at stations corresponding to 30 % to 70 % root chord and are denoted $x_m = 0.3$ to 0.7, respectively, where x_m is the measurement plane coordinate. A lateral coordinate y_m is defined normal to the leading-edge. The SPIV technique requires a calibration procedure to obtain the mapping function between the image coordinates and the physical space. This was obtained by using a two-level calibration pattern plate and the evaluation of the mapping function was made by LaVision DAVIS 7.1 software.

From the crossflow surveys the location of the starboard vortex axis was determined. In the second test campaign, the laser sheet was aligned with this axis and positioned normal to the wing. This setup, drawn schematically in Figure 4, enables to study the development of the flow in core axis direction. In this setup, one CCD camera is normal to the sheet and the second camera is at an angle of about 50° with the sheet.

C. Flow Seeding and Illumination

A SAFEX Fog generator produced a non-toxic water-glycol based fog consisting of droplets of approximately $1 \mu\text{m}$ in diameter. These were introduced into the wind tunnel flow downstream of the centrifugal fan of the wind tunnel.

A QUANTEL TWINS CFR 200 Nd:YAG laser emitted double light pulses of 200 mJ energy with a duration of $7 \mu\text{s}$ at a maximum repetition rate of 30 Hz. Through optics, the laser beam was converted into a 2 mm thick light sheet.

D. Imaging Recording and Data Processing

Two LaVision CCD cameras of 1376 x 1040 pixels were used to record the flow field. The two cameras are equipped with 60 mm focal length lenses and Scheimpflug adapters. Both lenses were equipped with daylight filters in order to reduce the background light in the SPIV images. A cross correlation method was used to obtain the velocity vector field from the reconstructed images.

Each flowfield measurement contained 100 records acquired at 1 Hz with a pulse separation time of 2 μ s. The flow is therefore not time resolved. Each image pair was analyzed with the La Vision Davis 7.1 software, applying the window deformation iterative multigrid technique¹⁹ with a final window size of 32 x 32 pixels and an overlap factor of 50 %. For visualization purposes only, the velocity vector field is low-pass filtered with a 3 x 3 Gaussian Kernel.

E. Oil Flow Technique

The direction of the boundary-layer flow on the leeward surface of the models was visualized using an oil-flow technique. The oil mixture consisted of titanium dioxide and kaolin powder (china clay) mixed with kerosene and pure oleic acid fluid. The mixture was applied with a soft brush on the surface of the models at freestream velocity. When dry, the surface flow pattern was photographed using a digital camera.

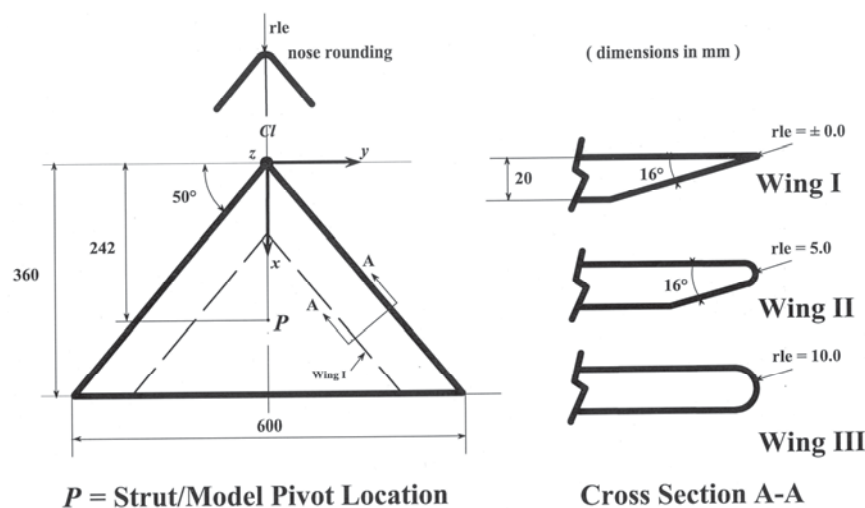


Figure 5. Planform and leading-edge shapes of large-scale models



Figure 6. Inverted model in LTT wind tunnel (side view)

The radius of the rounding at the nose is equal to that of the leading edge. The models have a square trailing edge and a

F. Wall Interference

Interpolation of the numerical predictions for the wall interference correction of a delta-type wing in a rectangular wind tunnel²⁰ indicates that the upflow angle correction for the small models is of the order of 1.5° at $\alpha = 15^\circ$. The models are actually positioned at a two chords distance from the tunnel exit. The upflow effects can therefore be expected to be less strong.

G. Accuracy of data

As far as the accuracy of the PIV measurements is concerned, in the free stream the uncertainty level of the velocity component is estimated to be 0.2 %. The uncertainty level is larger in regions with a high turbulence level such as the vortex core; the uncertainty of the velocities in the turbulent vortex core is estimated to be of the order of 3.0 %.¹³

With the PIV technique the flow velocity is measured indirectly by measuring the movement of particle tracers in the flow. As a consequence, in vortical flows particle lag also affects data accuracy. Based on Stokes drag law, a velocity lag of 1.0 % of the free stream velocity is estimated in the vortex core region at $x_m = 0.3$. The acceleration of the flow in the core region is found to decrease with distance x_m ; at $x_m = 0.7$ the velocity lag is estimated to be reduced to nil.

H. Models and Flow Facility used for Balance Measurements

The planform and edge shapes of the larger models are shown in Figure 5. The models were manufactured of 20-mm thick anodized Aluminum, have a chord length of 0.360 m and a span of 0.600 m. Wing I has a sharp leading edge of about zero radius. The bottom edge is beveled at 16°, which is slightly less than the bevel angle of the smaller models. Wing II has a semi-circular leading edge of 5.0 mm radius ($r_{le}/c = 0.0139$) and wing III a semi-circular edge of 10.0 mm radius ($r_{le}/c = 0.0278$), being half the model thickness. Similar to the small-scale models, the

thickness-to-chord ratio $t/c = 0.056$. The models were tested in the Low-Turbulence-Tunnel (LTT) of the Department of Aerospace Engineering of TUD. This is a closed-circuit tunnel with an octagonal test section 1.80-m wide, 1.25-m high and 2.60-m long. Most tests were conducted at an airspeed of about 50 m/sec, yielding an Re of about 1.2 million, but in order to be able to study Re -effects, for some α , in addition, data were acquired at $Re = 0.50, 0.97, 1.75$ and 2.17 million. Each model was suspended through a streamlined strut that was connected to a six-component balance system overhead of the test section (Figure 6). To avoid interference of the strut with the vortex flow, the wings were tested inverted, i.e. with their flat leeward surface facing down. In literature, it is common to present data of delta wings with their leeward surface facing up. This surface is then called the "upper" surface. This terminology is also used here.

Static time-averaged force-and-moment data were obtained using the six-component balance system. The data were taken at geometric α ranging from -6° to $+27^\circ$. The data were corrected for the elastic deformation of the strut and the balance system under aerodynamic load. Dummy measurements were performed to determine strut/model interference effects. The lift and drag coefficients C_L and C_D are based on freestream dynamic pressure and wing area. The pitching-moment coefficient C_m is, in addition, based on chord as reference length. This moment is taken relative to the strut/model pivot location P , marked in Figure 5.

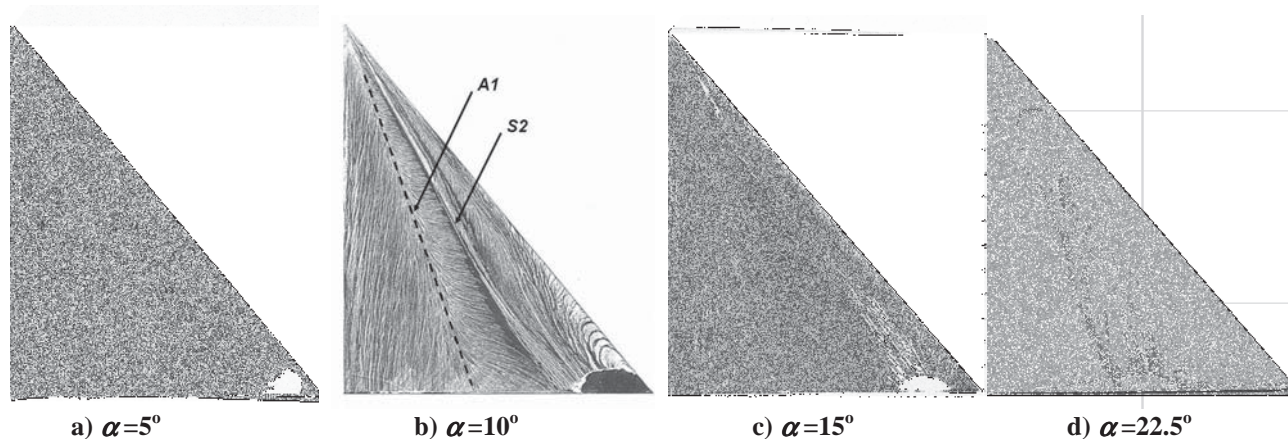


Figure 7. Effect of α on oil-flow pattern on leeward surface of wing I

As far as tunnel-wall-interference corrections are concerned, existing theories estimate corrections that can be applied for delta wings only if α is less than 25 deg, and if vortex breakdown does not take place over the wing.²⁰ The theory developed by Hsing and Lan²¹ has been used here to obtain an idea of the order of magnitude of the wall corrections.

Based on this theory, the upflow angle is estimated to be 0.5° at $\alpha = 5^\circ$ and to increase to about 2.7° at $\alpha = 25^\circ$. Based on the same theory, the blockage is estimated to be of the order of 4% at low α and to increase to about 6% at $\alpha = 25^\circ$. This blockage correction has been applied to the dynamic pressure used to non-dimensionalize the balance data. No special tests were carried out to determine the repeatability of the balance data. Comparison of data taken at identical (α, Re) combinations indicate a maximum uncertainty in C_L and C_D of 0.5 % and in C_m of 1.3 %.

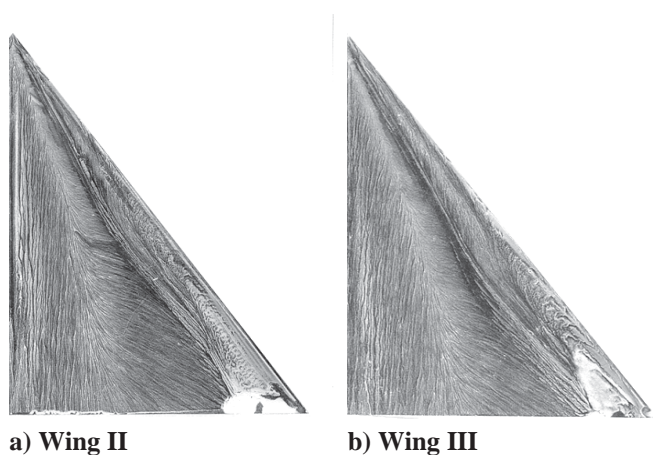


Figure 8. Oil-flow patterns at $\alpha = 15^\circ$

Figure 7 shows the oil-flow pattern on the starboard upper surface of small-scale model I at $\alpha = 5^\circ, 10^\circ, 15^\circ$ and 22.5° , respectively, for $Re = 2.0 \times 10^5$. At $\alpha = 5^\circ$, the

III. Test Results

A. Oil-flow visualization

flow separates at the leading edge forming a primary vortex that attaches at the primary-attachment line A_1 located at about $0.5 s$. The outward directed boundary layer separates at the secondary-separation line S_2 .

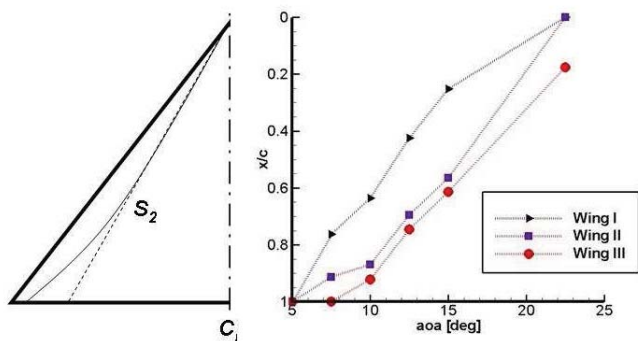


Figure 9. Effect of α on outward bending of S_2

Outboard of this line a secondary-attachment line is visible, suggesting the presence of a tertiary vortex. The secondary-separation line is straight up to the trailing-edge. At $\alpha = 10^\circ$, an outward bending of S_2 is visible upstream of the trailing edge. This outward bending is due to an enlargement of the primary-vortex footprint that is caused by vortex core breakdown. At $\alpha = 15^\circ$, the outward bending point has moved upstream to about $x/c = 0.25$. As will be shown in Section C. Flow data, the actual breakdown of the core occurs upstream of the bending point. At $\alpha = 22.5^\circ$, the primary-vortex footprint can be seen to be distorted by a fully turbulent boundary layer.

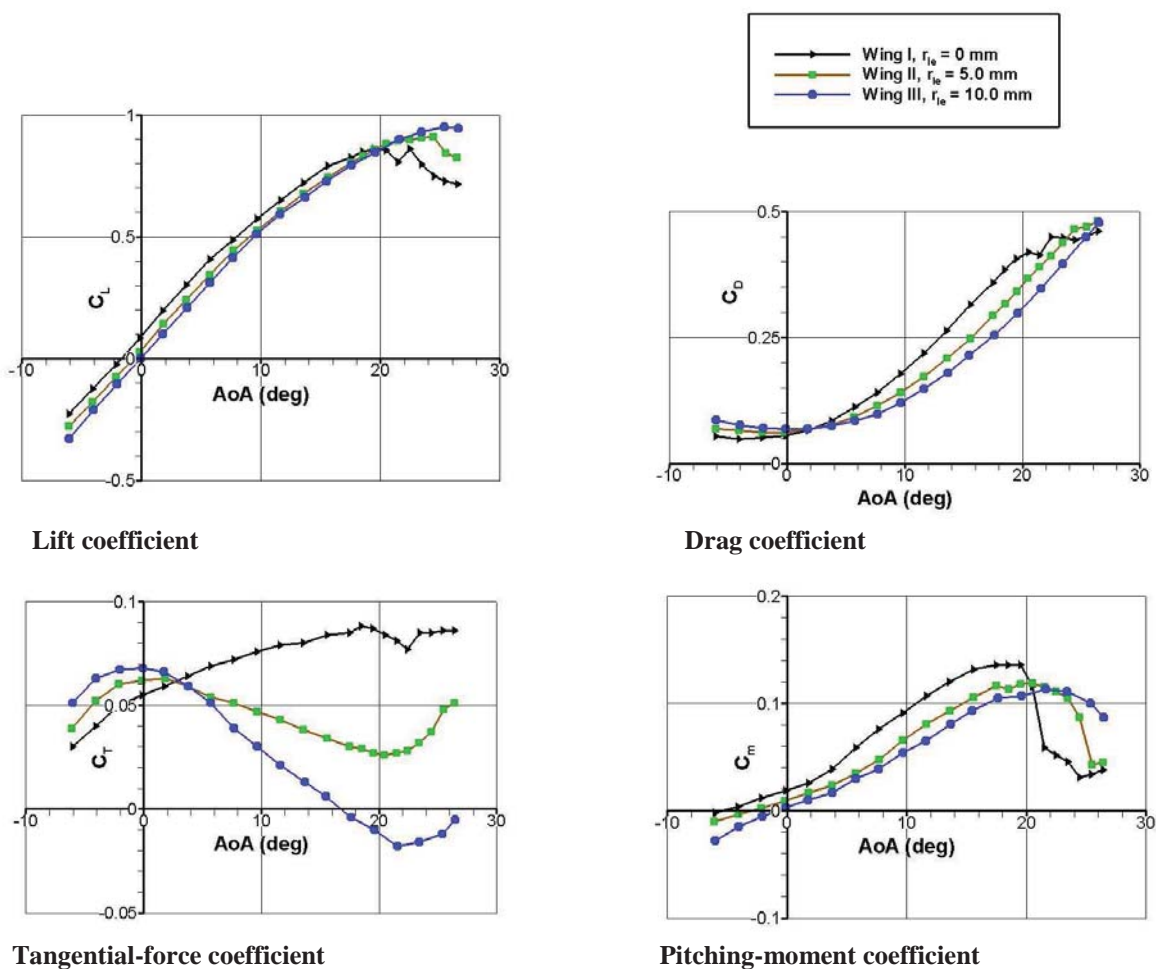


Figure 10. Balance data

Figure 8 shows the oil-flow pattern on wing II and III for $\alpha = 15^\circ$. Compared to wing I (Figure 7c), on wing II the outward bending of S_2 occurs more downstream. On wing III, the outward bending occurs again further downstream, suggesting that an increasing r_{le} will delay vortex breakdown. Renac et al¹⁶ observed a similar tendency on $\Lambda = 60^\circ$ delta wings and Huang et al²² on $\Lambda = 65^\circ$ delta wings.

Figure 9 shows the effect of α on the chordwise location of the outward bending point of S_2 for all the three wings. The data points were determined from the oil-flow patterns with an accuracy of $\pm 0.03 c$. The outward bending point on all three wings moves upstream with increasing α . An increase in r_{le} delays the outward bending of S_2 , which is indicative for a delay in the occurrence of vortex breakdown. Compared to wing I, depending on α , on wing II vortex breakdown occurs at a $0.10 c$ to $0.30 c$ more downstream location. Going from wing II to wing III, the rearward movement of the bursting point is less strong.

Cummings et al²⁴ compute the flowfield over a $\Lambda = 50^\circ$ UCAV configuration with rounded leading edges at a Re of the order of 10^5 . There is a correspondence between the computed upstream movement of the bursting point with α over the UCAV configuration and the upstream movement of the S_2 bending point observed over wing III.

Taylor et al⁴ investigated the flow over a 50° delta wing model in a water tunnel at Re ranging from 4,300 to 34,700. The model had a bottom-edge bevel of 45° , which is much larger than the bevel angle of the present models. In the range of Re tested, an upstream progression of the vortex bursting location was observed, which is interesting keeping in mind the insensitivity to Re of vortices and their bursting location over slender delta wings. In addition, with increasing Re an outboard shift of the vortex trajectory was observed. The observations in the water tunnel further suggest a less abrupt transition from coherent to broken vortex core at the higher Re .

B. Balance data

Figure 10 shows plots of balance data obtained on the larger models. The leading-edge radius can be seen to affect the level and slope of the force and moment coefficients. The level of C_L decreases with increasing r_{le} . Note that at $\alpha = 0^\circ$, $C_L = 0$ for wing III with its symmetrically rounded edges. The other two wings have edges that are beveled on the bottom side. The negative camber associated with this yields a positive C_L at $\alpha = 0^\circ$. The C_L of sharp-edged wing I increases linearly with α up to 5° . Beyond this angle, the slope of the C_L -curve reduces due to the occurrence of vortex breakdown over the model. The range of linear C_L - α extends when the edges of the model are rounded off. A strong lift loss can be noted at α beyond 20° when the burst approaches the apex. From Figure 9 it was noted that burst is delayed when the edges are rounded off. This explains why for the other two wings the strong lift loss occurs at a higher α .

As far as the drag coefficient is concerned, the increase in r_{le} results in a lower level of C_D . This is due to an increase in the leading-edge suction. When leading-edge separation occurs, a part of the leading-edge thrust goes into vortex lift, and a part into leading-edge suction. The interplay between the amount of vortex lift and leading-edge suction depends on the shape of the leading edge. On sharp-edged wing I, the vortex lift will dominate resulting in a large C_L . Rounding off the edges will increase the edge suction at the expense of the vortex lift. The latter is also evident from the C_T - α curves; as a result of the increasing suction, the a tangential force decreases with increasing r_{le} . The overall effect on the C_L -to- C_D ratio is that up to $\alpha = 6^\circ$ wing I has the largest ratio, while beyond this angle wing III dominates with the largest ratio at $\alpha = 10^\circ$.¹⁸

An effect of r_{le} can also be noted on the pitching-moment coefficient C_m ; the level of this coefficient increases with α and decreases with increasing r_{le} . Related to the strong decline in C_L , a strong decline in C_m can be observed again at α beyond 20° . The decline is delayed when the edges are rounded off.

The effects of Re on the balance data of the three models were reported earlier in Ref. 18. The data were acquired at α from 5° to 25° , in steps of 5° , and at Re ranging from 0.50 to 2.17 million. The effects of Re on the balance data turned out to be rather small, especially on C_D , and are expected to be mainly due to small changes in the vortex breakdown location with Re .

C. Flow data

The crossflow over the starboard halves of the three small-scale models was measured at $\alpha = 15^\circ$ and at a Re of 2.0×10^5 using the setup shown in Figure 2. The field-of-view dimensions were $66 \times 48 \text{ mm}^2$ at $x_m = 0.3$ and increased to $94 \times 72 \text{ mm}^2$ at $x_m = 0.7$. Data were taken at a mesh resolution $\Delta y = \Delta z = 0.76 \text{ mm}$ at $x_m = 0.3$, gradually increasing to $\Delta y = \Delta z = 1.00 \text{ mm}$ at $x_m = 0.7$. To give an idea of the resolution of the vortical flow, as will be shown below, the leading-edge vortex is smallest over wing III at $x_m = 0.3$. The vortex core at this station was resolved by a mesh consisting of 8×6 points. The number of mesh points that resolved the core increased with distance x_m . The largest vortex over wing III exists at $x_m = 0.7$ and was resolved by a mesh consisting of 30×22 points.

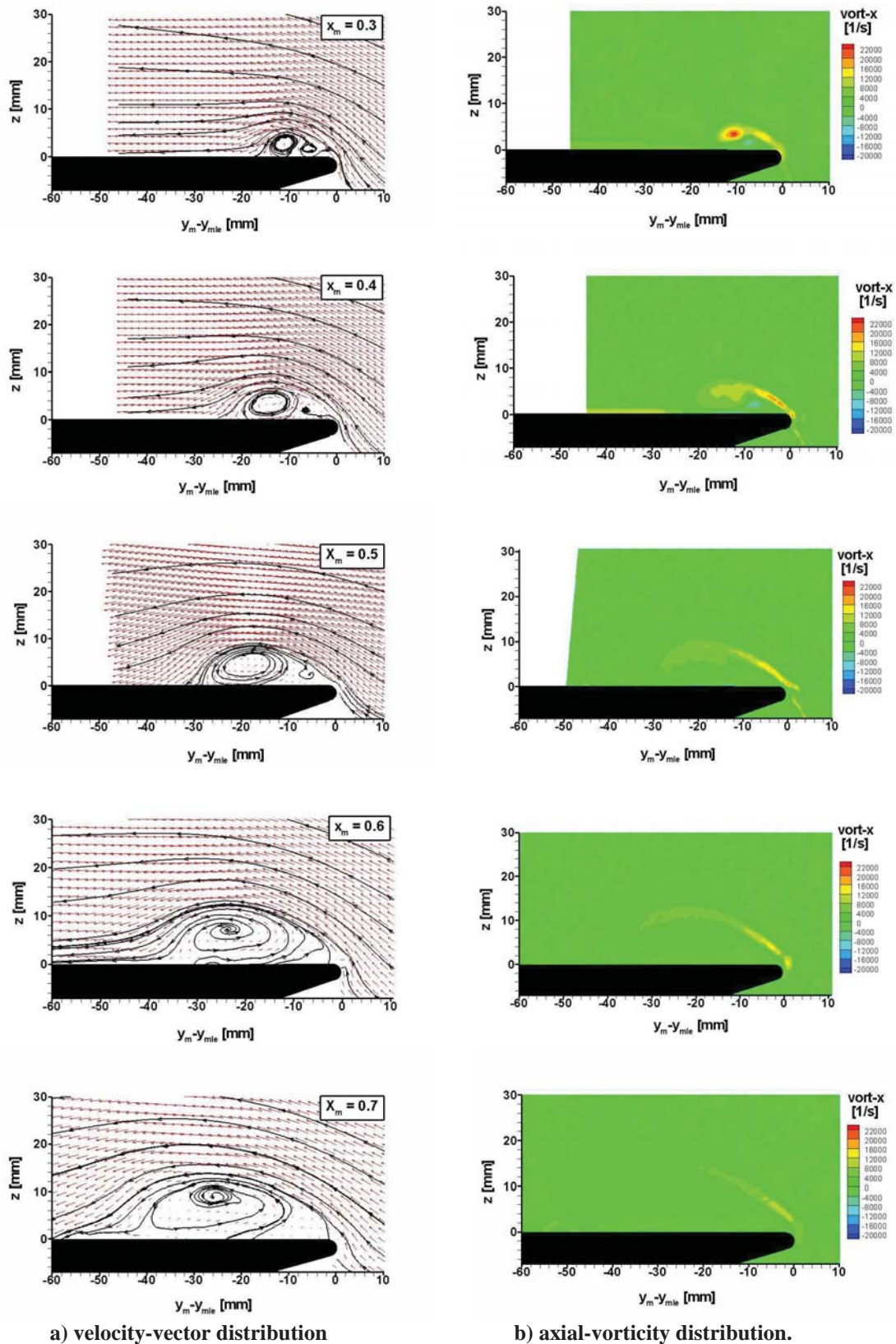


Figure 11. Chordwise development of crossflow over Wing II.

Figure 11 shows the development of the crossflow over wing II from $x_m = 0.3$ to 0.7. The left-hand plots show the time-averaged velocity-vector fields, the right-hand plots the contours of the axial-vorticity distribution as calculated from these fields. To avoid abundance of data, in the vector plots only half the number of data points is shown. The data is plotted versus $y_m - y_{mle}$, where y_m is the lateral coordinate in the measurement plane and y_{mle} the value of the coordinate at the wing leading edge. The plots show that the primary vortex increases in size with distance from the apex, because it is continuously fed with vorticity from the leading edge. Up to including $x_m = 0.5$, a small counter-rotating secondary vortex is visible outboard of the primary vortex. The mesh resolution was too low to resolve a tertiary vortex, if present. The crossflow data for wing I and III (not presented here) show also an increase in the size of the primary vortices with

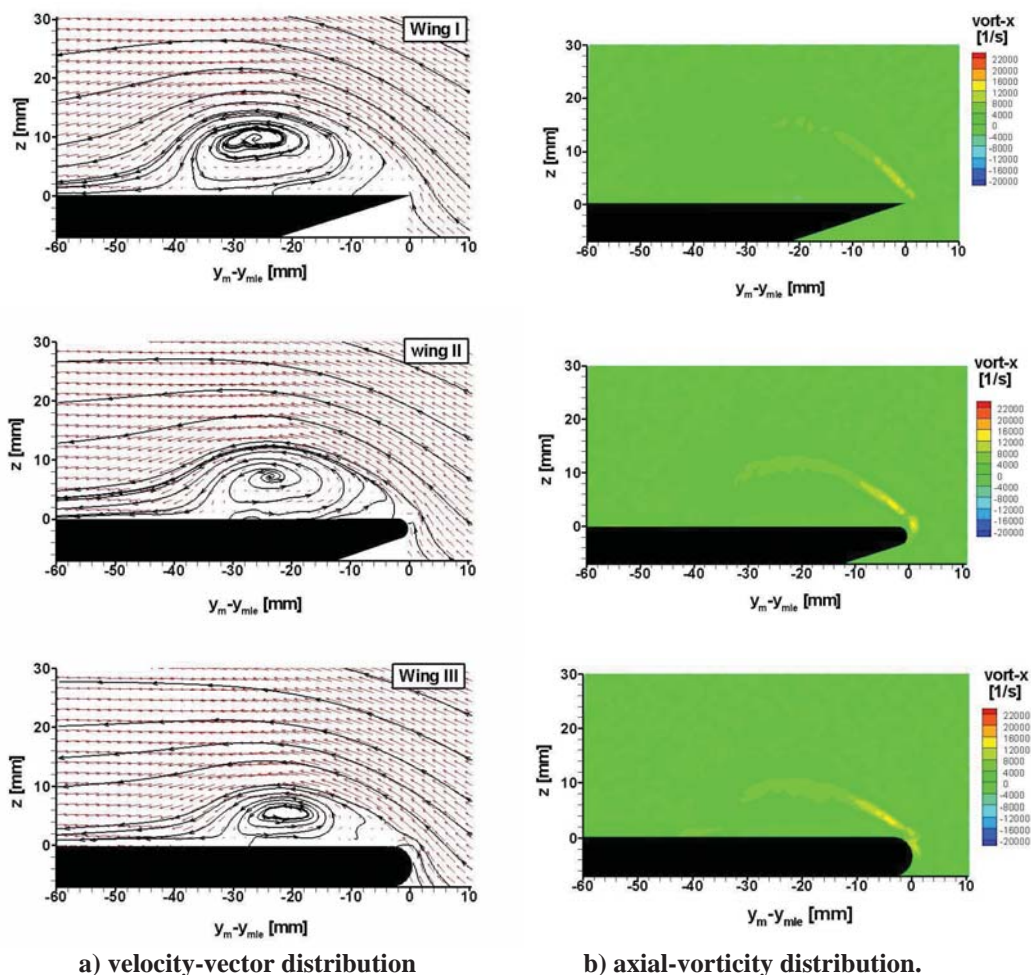


Figure 12. The crossflow over (from top to bottom) wing I to III at $\alpha = 15^\circ$; $x_m = 0.6$

distance x_m . On wing I no secondary vortex is detected, on wing III this vortex is too small to be resolved, if existing.

The axial vorticity on Wing II is largest in the core at $x_m = 0.3$. Downstream of this station, the level of the vorticity is decreasing. As will be clear later, this is due to breakdown of the core flow in this region. The time-averaged data show a smooth distribution of the vorticity in the free shear layer and no clear separate vortical substructures. Plots of the instantaneous axial vorticity were presented in a previous paper¹⁸. The plots did show the existence of separate vortical substructures in the free shear layer, indicating that this layer breaks up rapidly into a highly turbulent wake-type flow.

To illustrate the effect of the leading-edge radius on the crossflow over the three wings, in Figure 12 the flowfield data are compared that were measured in the plane $x_m = 0.6$. From wing I to wing III (increasing r_{le}), the vortex core can be seen to reduce in size and to move slightly outboard and closer to the wing surface. Associated with this is a reduction

in the angle of separation of the free shear layer. The axial-vorticity contours show a slight increase in the level of the vorticity in this layer.

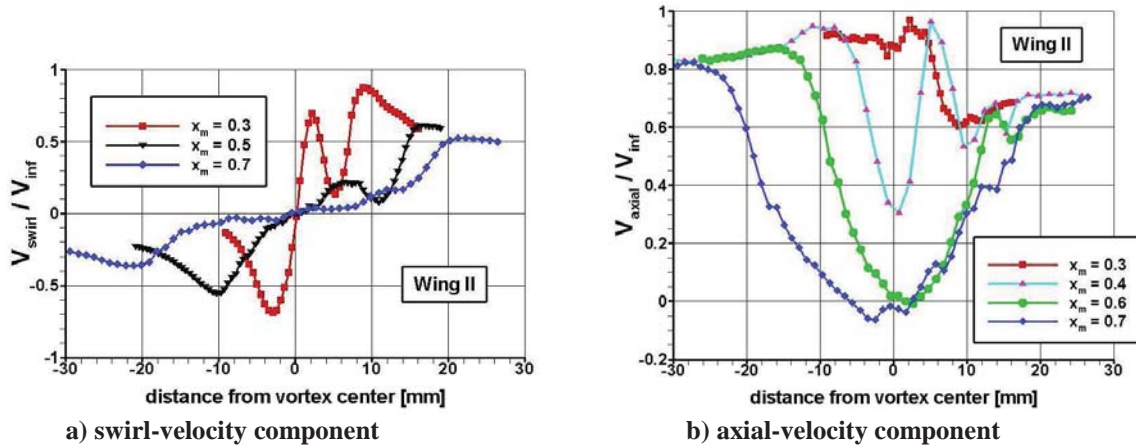


Figure 13. Chordwise development of velocity components over wing II; horizontal traverses through vortex axis at $\alpha = 15^\circ$.

Figure 13 shows the variation of the swirl- and axial-velocity component over wing II with distance x_m . It should be remarked that the swirl-velocity component was measured in the x_m crossflow plane, while the axial-velocity component is normal to this plane. The curves represent the distribution of these components along a horizontal traverse through the local vortex center. Note that the data are plotted relative to this center, and that the velocities have been non-dimensionalized by V_∞ (V_{inf} in the plots). The peaks of the swirl-velocity component can be seen to decrease strongly with increasing x_m , while the distance between the peaks – representing the vortex core width – can be seen to increase. The latter is also evident from the axial-velocity distributions. The axial velocity inside the core can be seen to reduce rapidly with increasing distance x_m . The swirl- and axial-velocity components for the other two wings show a similar behavior with the exception that there is a difference in the location where the drop in axial velocity starts to occur. This is illustrated with the next figure.

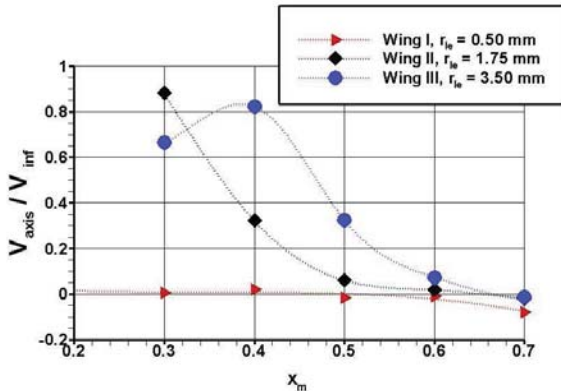


Figure 14. Variation of axial-velocity component along vortex axis.

Figure 14 shows how the axial-velocity component along the vortex axis V_{axis} changes with distance x_m . Wing III, with the full semi-circular edge, shows an increasing axial velocity up to $x_m = 0.4$. This is caused by the jet-like flow that exists in the core over the front part of this wing. The axial-vorticity contours for this wing (not presented here) show a concentrated vortex core at $x_m = 0.3$ and 0.4 , while further downstream the vorticity becomes diffuse due to the breakdown of the core flow. This phenomenon causes the decay in axial velocity and eventually a reverse flow at $x_m = 0.7$. This tendency confirms the predictions for the development of the axial flow over a $\Lambda = 50^\circ$ delta wing by Chen and Wang³. Because of the spiral-type of flow in the core, the effect of the breakdown on the surface flow will first be noted at a more downstream station; according to Figure 9 outward bending of S_2 is first observed at $x/c = 0.75$. The vorticity contour plots for wing II suggests a concentrated vortex core to exist only at $x_m = 0.3$ (Figure 11) and a fading core flow further downstream. This explains the rapid drop in the axial velocity along the core axis of this wing downstream of $x_m = 0.3$. The axial velocity at the core axis over wing I is almost zero first and becomes slightly negative downstream of $x_m = 0.5$. Extrapolation of the data from the other two wings suggests that breakdown over wing I would occur near its apex.

This above data confirm the earlier findings that a sharper leading edge promotes the breakdown of the core flow.

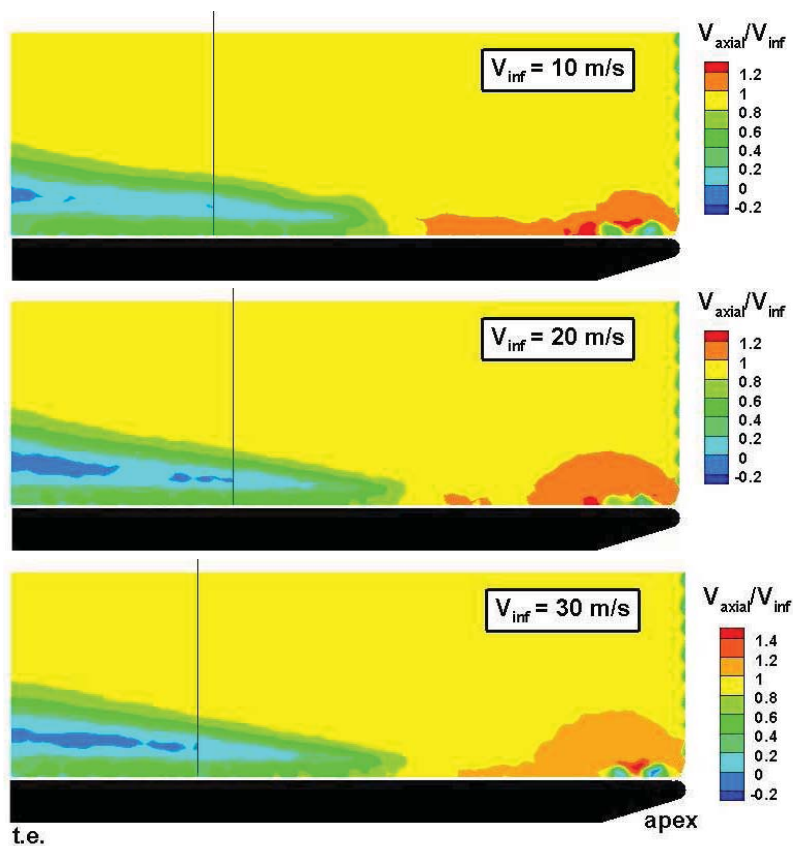


Figure 15. Axial-velocity contours over wing II for (from top to bottom) $Re = 1.0 \times 10^5$, 2.0×10^5 and 3.0×10^5 .

Figure 15 shows the contours of the axial-velocity component measured in a plane normal to the surface of wing II. The setup for this measurement was given in Figure 4. The measurement plane passes through approximately the axis of the starboard primary vortex. Approximately, since the vortex axis is not straight. A exact comparison with the data plotted in Figure 14 is therefore not possible. The contours were measured, from top to bottom, at three $Re = 1.0 \times 10^5$, 2.0×10^5 and 3.0×10^5 ($V_\infty = 10$, 20 and 30 m/s), respectively. The Re -range is limited due to the velocity range of the wind tunnel.

Near the apex at $x_m = 0.05$, a mean axial velocity of $1.15 V_\infty$ is measured at $Re = 2.0 \times 10^5$. The vortex is formed in this region and a jet-type flow exists in the core. Surprisingly, both a decrease and increase of Re were found to give a larger axial velocity (1.30 and $1.48 V_\infty$, respectively). A delay in the axial velocity at approximately $x_m = 0.40$ marks the breakdown of the core flow. A slightly more upstream location was found in Figure 14. As mentioned above, this is because the measurement plane did not pass exactly through the vortex axis.

In the contour plots, a black vertical line marks the location where the axial velocity eventually becomes negative. A weak dependence on Re of this location can be observed. The latter was also found in the contours of the axial-velocity along the core axis of wing I and III.

Near the apex of sharp-edged wing I at $x_m = 0.05$, a mean axial velocity of $1.31 V_\infty$ was measured at $Re = 2.0 \times 10^5$. In both the predictions by Gordnier et al⁷ and the experiment by Taylor et al⁴ axial velocities of over $2.0 V_\infty$ were acquired

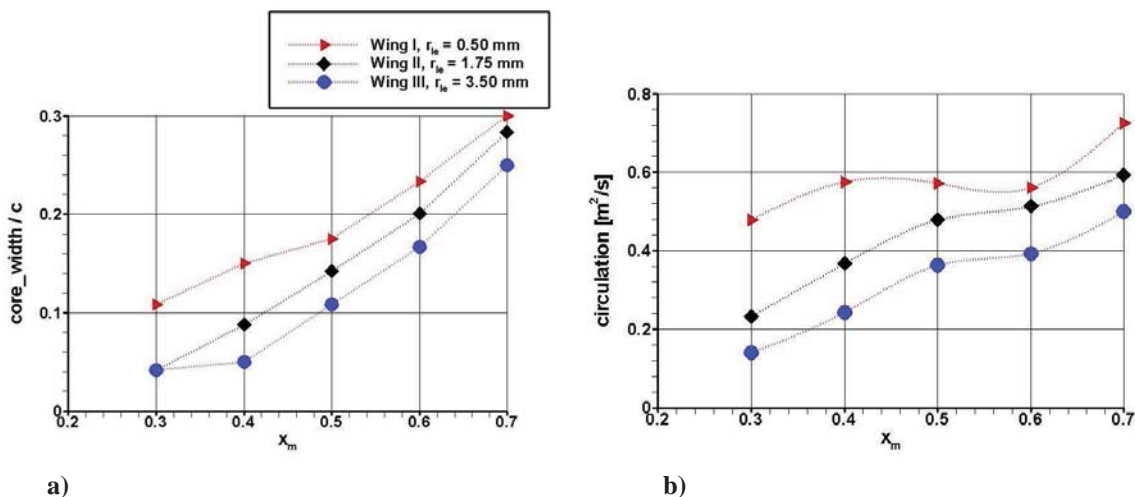


Figure 16. Variation of a) vortex core width and b) circulation about vortex core with distance x_m .

near the apex of a $\Lambda = 50^\circ$ delta wing. It should be reminded though, that the edge shape of their delta wing is different from the one used here.

The crossflow data for the three wings was processed further to quantify the effect of the distance x_m on the core width and on the circulation about this core.

Figure 16a shows the effect on the dimensionless vortex core width. The core width is defined to be the distance between the peaks of the swirl-velocity component. The core over the three wings can be seen to grow continuously with x_m . A larger leading-edge radius results into a thinner vortex over the wing.

The circulation about the elliptical vortex core was estimated using the distributions of the swirl-velocity component along a y_m - and z -traverse through the local vortex center. Results are given in Figure 16b. The circulation is largest over sharp-edged wing I. This is mainly due to the fact that this wing has the largest core. A reduction of the circulation is clearly visible beyond $x_m = 0.4$. This is supposed to be caused by the breakdown of the core flow more upstream. Surprisingly, from $x_m = 0.6$ the circulation can be seen to increase again.

A larger leading-edge radius can be noted to result into a weaker vortex. The circulation about the vortex core over wing II and III increases almost linearly up to $x_m = 0.5$. Beyond this station, the curves for both wings show a reduction of the slope.

IV. Conclusions

A study is presented of the effects of the leading-edge radius on the flow over $\Lambda = 50^\circ$ delta wing models.

The oil-flow visualization shows a clear effect of the leading-edge radius on the location of the secondary-separation line; a larger radius delays the outward bending of the secondary-separation line, which is indicative for a delay in the occurrence of vortex core breakdown over the models.

The SPIV data shows that a larger leading-edge radius reduces the size and strength of the primary vortex and moves this vortex outboard and closer to the wing surface.

In the limited Re -range tested, only a weak dependence on Re of the core breakdown location is observed.

The balance data shows that the leading-edge radius affects the level and slope of the forces acting on the wings. Changes in the slope of the curves are caused by vortex breakdown displacements. At α beyond 20° , vortex breakdown occurs over the entire wing resulting in a strong loss of lift and pitching moment. This loss is delayed to a higher α , when the edges of the wing are rounded off. The effects of Re on the balance data are small,

Acknowledgements

The author would like to thank Mr. Frits Donker Duyvis from the Faculty of Aerospace Engineering of TUD for preparing the SPIV equipment, and Associate Prof. Xia Lu from NWPU, China, for performing the SPIV tests.

References

1. Gursul, I., Gordnier, R. and Visbal, M., "Unsteady Aerodynamics of Nonlender Delta Wings," *Progress in Aerospace Sciences* 41, 2005, pp. 515-557.
2. Gordnier, R.E. and Visbal, M.R., "High-Order Compact Difference Scheme applied to the Simulation of a Low Sweep Delta Wing Flow," AIAA 2003-0620, January 2003.
3. Chen, L. and Wang, J.J., "Numerical Simulations of Leading-Edge Vortex Core Axial Velocity for Flow over Delta Wings," *Science in China Series E: Technological Sciences*, July 2009, Vol. 52, 7, pp. 2029-2036.
4. Taylor, G.S., Schnorbus, T. and Gursul, I., "An Investigation of Vortex Flows over Low Sweep Delta Wings," AIAA 2003-4021, June 2003.
5. Wang, J.J. and Zhang, W., "Experimental Investigations on Leading-Edge Vortex Structure for Flow over Non-Slender Delta Wings," *Chinese Physical Letters*, Vol. 25, No. 7 (2008) 2550.
6. Lambourne, N.C. and Bryer, D.W., "The Bursting of Leading-Edge Vortices – Some Observations and Discussion of the Phenomenon," Aeronautical Research Council R&M. 3282, April 1961.

7. Gordnier, R.E., Visbal, M.R., Gursul, I. and Wang, Z., "Computational and Experimental Investigation of a Non slender Delta Wing," AIAA 2007-0894, January 2007.
8. Chu, J. and Luckring, J., "Experimental Surface Pressure Data obtained on 65° Delta Wing across Reynolds Number and Mach number Ranges," NASA Technical Memorandum 4645, 1996.
9. Henderson, P.W., "Effects of Wing Leading-Edge Radius and Reynolds Number on Longitudinal Aerodynamic Characteristics of Highly Swept Wing-Body Configurations at Subsonic Speeds," NASA TN D-8361, 1976.
10. Rinoie, K., "Experiments on a 60-Degree Delta Wing with Rounded Leading-edge Vortex Flaps", *Journal of Aircraft*, Vol.37, No.1, 2000, pp. 37-44.
11. Kegelman, J.T. and Roos, F.W., "Effects of Leading-Edge Shape and Vortex Burst on the Flowfield of a 70-Degree-Sweep Delta Wing," AIAA 89-0086, January 1989.
12. Lawson, M.V. and Riley, A.J., "Vortex Breakdown Control by Delta Wing Geometry," *Journal of Aircraft*, Vol. 32, No. 4, 1995, pp. 832-838.
13. Verhaagen, N.G. and VanBossuyt, C., "Flow on a 65-Deg Blunt Apex," AIAA 2006-2005, June 2006.
14. Chiba, K., Obayashi, S. and Nakahashi, K., "CFD Visualization of Second Primary Vortex Structure on a 65-Degree Delta Wing," AIAA 2004-1231, January 2004.
15. Luckring, J.M. and Hummel, D., "What was learned from the new VFE-2 Experiments," AIAA 2008-0383, January 2008.
16. Renac, F., Barberis, D. and Molton, P., "Control of Vortical Flow over a Rounded Leading-Edge Delta Wing," *AIAA Journal*, Vol. 43, No. 7, July 2005, pp. 1409 – 1418.
17. Matsuno, T. and Yakamura, Y., "Self-Induced Roll Oscillation of 45-Degree Delta Wings", AIAA 2000-0655, January 2000
18. Verhaagen, N.G., "Effects of Leading-Edge Radius on Aerodynamic Characteristics of 50° Delta Wings," AIAA 2010-0323, January 2010.
19. Scarano, F. and Riethmuller, M L. "Iterative multigrid approach in PIV image processing," *Exp. Fluids*, 26, 1999, pp. 513–523.
20. Verhaagen, N.G., "Tunnel Wall Effect on the Flow Around a 76/40-deg Double-Delta Wing," AIAA Paper 98-0312, Jan. 1998.
21. Hsing, C.-C. A. and Lan, A.E., "Low-Speed Wall Interference Assessment/Correction with Vortex Flow Effect," *Journal of Aircraft*, Vol. 34, No. 2, 1997, pp. 220-227.
22. Huang, X.Z., Mébarki, Y., Benmeddour, A. and Brown, T., "Experimental and Numerical Studies of Geometry Effects on UCAV's Aerodynamics," AIAA 2004-0403, January 2004.
23. Konrath, R., Klein, C. and Schröder, A., "PSP and PIV Investigations on the VFE-2 Configuration in Sub- and Transonic Flow," AIAA 2008-379, January 2008.
24. Cummings, M.R., Morton, S.A., Siegel, S.G. and Bosscher, S., "Numerical Prediction and Wind Tunnel Experiment for a Pitching Unmanned Combat Air Vehicle," AIAA 2003-0417, January 2003.